

Dynamic measures of regional lung air volume using phase contrast x-ray imaging

M J Kitchen¹, R A Lewis¹, M J Morgan¹, M J Wallace³, M L Siew³,
K K W Siu^{1,2}, A Habib¹, A Fouras⁴, N Yagi⁵, K Uesugi⁵ and S B Hooper³

¹ School of Physics, Monash University, Melbourne VIC 3800, Australia

² Monash Centre for Synchrotron Science, Monash University, Melbourne VIC 3800, Australia

³ Department of Physiology, Monash University, Melbourne VIC 3800, Australia

⁴ Division of Biological Engineering, Monash University, Melbourne VIC 3800, Australia

⁵ Spring-8/JASRI, Sayo, Hyogo 679-5198, Japan

E-mail: Marcus.Kitchen@sci.monash.edu.au

Received 22 May 2008, in final form 5 September 2008

Published 8 October 2008

Online at stacks.iop.org/PMB/53/6065

Abstract

Phase contrast x-ray imaging can provide detailed images of lung morphology with sufficient spatial resolution to observe the terminal airways (alveoli). We demonstrate that quantitative functional and anatomical imaging of lung ventilation can be achieved *in vivo* using two-dimensional phase contrast x-ray images with high contrast and spatial resolution ($<100\ \mu\text{m}$) in near real time. Changes in lung air volume as small as $25\ \mu\text{L}$ were calculated from the images of term and preterm rabbit pup lungs ($n = 28$) using a single-image phase retrieval algorithm. Comparisons with plethysmography and computed tomography showed that the technique provided an accurate and robust method of measuring total lung air volumes. Furthermore, regional ventilation was measured by partitioning the phase contrast images, which revealed differences in aeration for different ventilation strategies.

 This article features online multimedia enhancements

(Some figures in this article are in colour only in the electronic version)

1. Introduction

The early detection and treatment of lung diseases are greatly restricted by the inability to dynamically image the lung *in vivo* with high contrast and spatial resolution ($<100\ \mu\text{m}$), particularly the small airways that harbour many of the pathologies associated with lung disease. As a result, most lung diseases are usually undetectable until the disease has progressed sufficiently such that a reduction in the respiratory function becomes clinically evident.

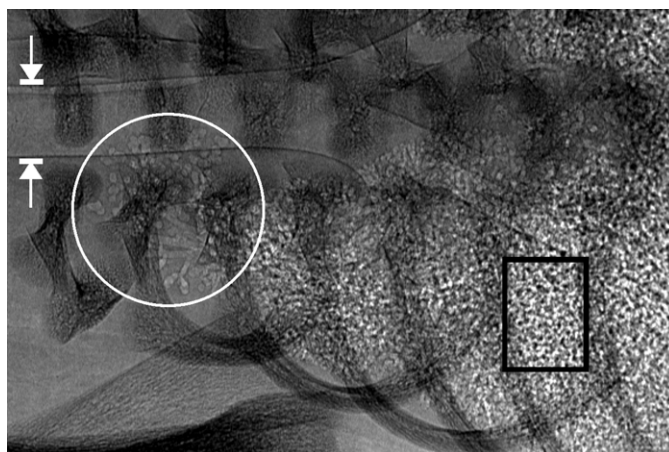


Figure 1. High resolution ($12\ \mu\text{m}$ pixels) image of a newborn rabbit foetus acquired with propagation-based phase contrast x-ray imaging using 25 keV x-rays and a 2 m object-to-detector distance. This image was acquired at beamline 20B2 at the SPring-8 synchrotron in Japan. Arrows indicate the edges of the trachea that are rendered visible by phase contrast. Bronchi can be seen branching from the trachea about half-way along the image. The white circle highlights a region of the lung where individual terminal airways are directly observable. Deep within the lung, many airways overlap in projection to create a speckled intensity pattern (Kitchen *et al* 2004), as seen within the black rectangle. In small animals, these features are not readily observed *in situ* using x-ray attenuation contrast alone (Lewis *et al* 2005, Kitchen *et al* 2005a, Yagi *et al* 1999). Image size: $72 \times 48\ \text{mm}^2$.

Attenuation-based x-radiography is commonly used to image the lung, but only provides low contrast images of lung tissue and yields no quantitative information about lung morphology or function. Other lung imaging modalities include computed tomography (CT) (Bartling *et al* 2007, Ford *et al* 2007, Namati *et al* 2006, Hu *et al* 2004, Schuster *et al* 2004), magnetic resonance imaging (Driehuys and Hedlund, 2007, Schuster *et al* 2004), K-edge subtraction imaging (Bayat *et al* 2001, Monfraix *et al* 2005), positron emission tomography (Schuster *et al* 2004) and electrical impedance tomography (Frerichs *et al* 2003). These modalities can provide high contrast images of the lung but often require the inhalation of contrast gases and suffer poor spatial and/or temporal resolution.

Phase contrast x-ray imaging utilizes partially coherent radiation (Wilkins *et al* 1996) and can produce high contrast images of the lungs with high spatial ($<100\ \mu\text{m}$) and temporal ($<100\ \text{ms}$) resolutions without a contrast agent (Yagi *et al* 1999, Suzuki *et al* 2002, Lewis *et al* 2003, Kitchen *et al* 2004, 2005a, Lewis *et al* 2005, Hooper *et al* 2007, Westneat *et al* 2003). Image contrast is enhanced by exploiting variations in an object's refractive index to highlight the boundaries between media of different refractive indices. A prominent variation in the refractive index occurs at each of the numerous air/tissue boundaries of the lung, which makes it an ideal organ for phase contrast imaging (Kitchen *et al* 2004, 2005a). Figure 1 provides an example of phase contrast imaging of the lung.

Herein we describe and validate a new technique for extracting quantitative volumetric information from single projection phase contrast x-ray images of the lung *in vivo*. We demonstrate its use on neonatal rabbit pups for dynamically measuring regional changes in lung air volumes during both artificial lung inflations and spontaneous breathing. We have used simultaneous plethysmography to demonstrate the accuracy of this technique for providing quantitative information on total lung gas volumes. In combination, the imaging

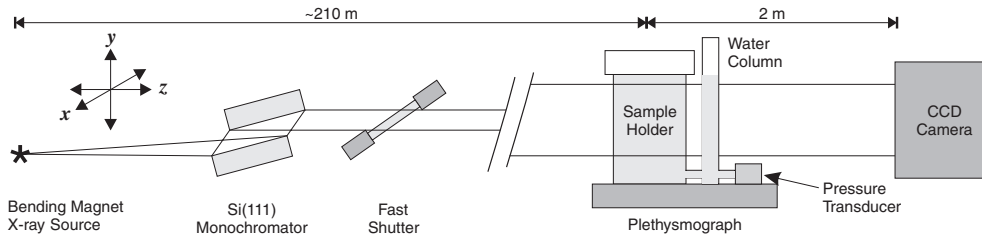


Figure 2. Schematic of the geometry for propagation-based phase contrast x-ray imaging, which shows the water plethysmograph used to independently measure lung air volume.

and analytical techniques can provide high resolution images of the lung alongside measures of regional changes in lung gas volumes on a breath-by-breath basis.

2. Materials and methods

2.1. Volumetric reconstruction from 2D images

Digitized, single projection x-ray images can be used to accurately measure the volume of an object comprised of a single homogeneous material when using a monochromatic x-ray source. Define a coordinate system such that the x-rays propagate along the z -direction (figure 2). From the digital images, the projected thickness $t(x, y)$ of the object can be readily calculated at each pixel using the Beer–Lambert attenuation law and the material’s known linear attenuation coefficient (μ_l). Summing the projected thickness over each pixel yields the object’s volume. Changes in the object’s volume with time can then be calculated from differences within a dynamically recorded image sequence:

$$\Delta V = \left(\sum_{i=1}^M \sum_{j=1}^N t(x_i, y_j) (\Delta x)^2 \right)_n - \left(\sum_{i=1}^M \sum_{j=1}^N t(x_i, y_j) (\Delta x)^2 \right)_{n=1}, \quad n = 1, 2, 3, \dots, \quad (1)$$

where i and j are discrete indices of the $M \times N$ pixels, Δx is the pixel size and n is the frame number of the image sequence.

For propagation-based phase contrast x-ray imaging, a form of in-line holography (Wilkins *et al* 1996, Yagi *et al* 1999, Kitchen *et al* 2005a), volumetric information can be calculated by first applying a single-image phase retrieval algorithm, such as that described by Paganin *et al* (2002), to reconstruct the object’s projected thickness:

$$t(x, y) = -\frac{1}{\mu_l} \ln \left(\mathbf{F}^{-1} \left[\mu_l \frac{\mathbf{F} [M_S^2 I(x/M_S, y/M_S, z)] / I_o(x, y)}{z_o \delta M_S (k_x^2 + k_y^2) + \mu_l} \right] \right). \quad (2)$$

Here, \mathbf{F} represents the discrete Fourier transform, M_S is the image magnification resulting from point-source illumination, I is the measured intensity, I_o is the incident intensity, k_x and k_y are spatial frequencies in the x - and y -directions, respectively, z_o is the object-to-detector distance and δ is the refractive index decrement for the single homogeneous material. Note that equation (2) is a corrected form of that derived by Paganin *et al* (2002), due to a rearrangement of the magnification factors. This algorithm decodes the phase contrast in the image so as to yield the projected thickness of material in the sample, reducing to the well-known Beer–Lambert law in the limit as z_o tends to zero. If the approximations of the algorithm are satisfied, we expect a more accurate reconstruction of the projected thickness at

the boundaries between objects since the phase contrast signal enhances the contrast-to-noise ratio (CNR) at the boundaries. Moreover, as z_o increases, incoherently scattered radiation becomes increasingly less likely to reach the detector, which further improves the CNR and therefore the accuracy of the reconstructed thickness.

Equation (2) requires that the object satisfy the projection approximation, for which the lateral shifts of the x-ray wavefield due to refraction within the material must be small. Previous studies employed ray tracing simulations to show that the projection approximation is well satisfied for imaging the lungs of small animals under experimental conditions similar to those used here (Kitchen *et al* 2004). Moreover, Kitchen *et al* (2004) showed that the geometrical optics approximation can be used to explain the contrast seen in the phase contrast images of small animal lungs under the same conditions, further validating the use of equation (2) for these images.

If an object is comprised of multiple materials and the volume of just one homogenous material changes with time, then the volume change of that material can be accurately calculated by assuming that the entire object is comprised of the one material, provided the approximations of the phase retrieval algorithm are satisfied, as we demonstrate herein. Changes in lung gas volumes cannot be directly measured using (1) and (2) since the total attenuation through the thorax will not change as the lungs inflate/deflate. A solution is to employ the Archimedean principle of volume measurement via fluid displacement. In this instance, a volume of water within the imaging field of view is displaced by an equal change in lung gas volume during ventilation. This is analogous to the more conventional method of measuring lung aeration via fluid displacement, namely plethysmography. In our experiments, newborn rabbit pups were placed, head-out, in a water-filled Perspex plethysmograph to directly measure the change in total lung gas volume for comparison with volumes calculated from phase contrast image sequences (figure 2). An image partitioning procedure was then used to calculate regional lung volumes from the images.

2.2. Phase contrast imaging

All objects were imaged in Hutch 3 of beamline 20B2 at the SPring-8 synchrotron radiation source, Japan (Goto *et al* 2001). Objects were placed approximately 210 m downstream of the source with the detector positioned a further 2 m downstream. A Si(1 1 1) double-bounce monochromator filtered the broad-spectrum bending magnet radiation. The large source-to-detector distance provided a beam size approximately 300 mm wide by 30 mm high, which was sufficiently large to image the entire thorax of the rabbit pups in a single exposure, enabling dynamic sequences to be recorded without scanning the object through the beam (figure 2). The large source-to-detector distance and monochromaticity ensure a highly spatially and temporally coherent beam, establishing ideal conditions for phase contrast imaging (Goto *et al* 2001).

Two experiments were conducted at separate times, between which the imaging energy and detector were optimized to increase the CNR. The first experiment utilized a 25 keV x-ray beam and a 25 μm thick gadolinium oxysulfide ($\text{Gd}_2\text{O}_2\text{S}$) phosphor-coupled CCD camera (Hamamatsu, C4742-95HR), with a tandem lens system providing an effective pixel size of 22.47 μm (2×2 pixel binning) and a 44.94 (H) \times 29.48 (V) mm^2 field of view. This beam energy and detector combination was previously found to provide high contrast images of lung tissue with sufficient resolution to observe alveoli within small animals (Lewis *et al* 2005, Hooper *et al* 2007).

The absorption-based CNR was later tested as a function of energy between 20 keV and 34 keV. The contrast between the central (thickest) part of the water-filled plethysmograph and

the direct beam, normalized by the noise level at the centre of the plethysmograph, was greatest at 24 keV on this beamline using the 25 μm thick phosphor. By decreasing the energy from 25 keV to 24 keV, the average CNR increased by $11 \pm 7\%$ with a concomitant increase in dose of around 7%. Since the experiments were terminal, contrast enhancement was considered of primary importance. The CNR was further improved by using an electron-multiplying CCD camera (Hamamatsu, C9100-02), with a gain setting of 100 providing a high CNR. The tandem lens system provided an effective pixel size of 31.82 μm (2×2 pixel binning) and a 31.82 (H) \times 31.82 (V) mm^2 field of view. Although the exact increase in the CNR with this detector is still to be quantified, this system enabled the acquisition of high contrast images of the lungs with sufficient CNR and spatial resolution to reveal the minor airways with exposure times as low as 50 ms.

2.3. Animal experimental procedures

All procedures involving animals were approved by the Monash University Animal Ethics Committee and the SPring-8 Animal Care and Use Committee. Pregnant New Zealand white rabbits ($n = 10$) at 31 days of gestation were anaesthetized by an intravenous injection of propofol (Rapinivet; 12 mg kg^{-1} bolus, 40 mg h^{-1} infusion). Pups were delivered by the caesarean section and randomly allocated into two groups. Pups in the first group ($n = 22$) were humanely killed via anaesthetic overdose before taking their first breath (foetus). Following death an endotracheal tube was inserted, via a tracheotomy, into the mid-cervical trachea and connected to an air-filled syringe. The syringe plunger was remotely controlled using a pre-calibrated syringe driver. The lungs were inflated by continuous infusion of air, with images acquired at regular time intervals. The plethysmograph recorded the change in lung gas volume directly by measuring the volume of water displaced from the main chamber into a water column (figure 2). The volume of displaced water was measured using a pressure transducer and recorded digitally using a data acquisition system (Chart, ADI, Sydney, Australia). This system was calibrated by measuring the pressure increase caused by the injection of a known volume (1 ml) of water. The shutter (figure 2) opening period was recorded simultaneously with the pressure recordings to indicate approximate (± 20 ms) image acquisition times.

Pups in the second group ($n = 6$) were imaged live from birth. Upon delivery, they were immediately placed in the pre-warmed (37 $^{\circ}\text{C}$) water-filled plethysmograph (figure 2) that was sealed at the top with a stiff rubber diaphragm. The head of each pup was located outside the plethysmograph chamber and the diaphragm formed a seal around its neck. Images were acquired as quickly as practical in an attempt to record the first breaths. The exposure time was limited to 50 ms to minimize motion blurring, with an inter-frame time of 600 ms. The fast shutter was used between exposures to minimize the x-ray dose delivered to the pups. The energy-dependent surface entry dose was calculated for the imaging sequences based upon the known exposure factors at the object position using the Si(1 1 1) monochromator (Goto *et al* 2001) and the exposure times.

2.4. Image analysis

Custom software was used to subtract the detector dark current offset and to normalize the CCD counts by the intensity incident on the sample. This was achieved by averaging several dark field images recorded with the x-ray shutters closed and flat field images with no object present after each image sequence was acquired. For sequences longer than a few minutes the fluctuations in incident beam intensity, arising primarily from thermal fluctuations in the

monochromator, had to be accounted for in the reconstruction. Small image segments not containing the object of interest were used to normalize the intensity in each frame to the first frame of the sequence.

In each sequence, the volume of water displaced between frames was determined using (1) and (2). For multi-material samples, only the change in volume of one material can be accurately measured. For these relative measures, the volume measured from the first image is subtracted from subsequent images; hence, the initial volume is offset to zero. Equation (2) exploits the known energy-dependent attenuation coefficient (μ_l) and refractive index decrement (δ) of water. The NIST database (NIST 2007) provided μ_l values of 54.8 m^{-1} and 50.7 m^{-1} (including coherent scattering) for 24 keV and 25 keV x-ray energies, respectively. At these energies, δ was calculated as 4.00×10^{-7} and 3.81×10^{-7} using the standard formalism (see, e.g., Kitchen *et al* 2004).

Regional lung air volume measurement was achieved using a simple image partitioning procedure. The chest cavity was divided into quadrants using the spinal column to separate the left and right lungs and the seventh rib to separate the apical and basal lobes. Fixing the regions of interest to the ribs was essential such that the same fraction of bone remained in each partition to satisfy the single-material assumption. Partitioning was performed after the projected thickness was calculated for each image. Since the lungs inflate/deflate during ventilation, buoyancy forces moved the pups within the plethysmograph, necessitating vertical motion tracking. For the sequence shown in figure 5, cross-correlation analysis provided an automated method of tracking the pup's displacement. Motion blurring artefacts associated with imaging live pups (figure 6) made cross-correlation analysis impractical; hence, motion tracking was performed manually after each inspiratory effort.

Lung volume measurements were also compared with high resolution computed tomography scans acquired on the same synchrotron beamline as the phase contrast image sequences. For each CT set, 1200 projections were recorded using 25 keV x-rays with a pixel size of $22.47 \mu\text{m}$. Slices were reconstructed using a filtered-backprojection algorithm with a Hanning filter. The airway volume was calculated by thresholding the reconstructed images to discriminate air from surrounding soft tissue. Summing over the air-filled pixels in each slice enabled a calculation of the total lung air volume.

3. Results

3.1. Proof of principle

Before demonstrating the application of the technique to lung volume measurement, a simple example is provided to show that (1) and (2) can successfully measure volume changes of a single material embedded within a multi-material object. A phase contrast image sequence of a domestic-grade synthetic sponge was acquired as it absorbed water supplied via a syringe pump at an infusion rate of 2.0 ml min^{-1} (figure 3). As the sponge filled with water, the transmitted intensity reduced due to increased x-ray attenuation, whilst strong phase contrast fringes appeared at the boundaries of air pockets trapped within the sponge. Figure 3(c) shows the change in water volume calculated from the image sequence using (1) and (2). The mass of added water was measured using a digital balance and calculated as $2.787 \pm 0.001 \text{ ml}$ at STP. The images revealed that the water flowed for $88 \pm 1 \text{ s}$, yielding an average flow rate of $1.9 \pm 0.1 \text{ ml min}^{-1}$. A theoretical (expected) curve, based upon a flow rate of 1.9 ml min^{-1} , is provided in figure 3(c). The mean difference between the measured and expected curves is 0.038 ml with a standard deviation of 0.044 ml . The correlation is highly statistically significant despite the object being comprised of multiple materials.

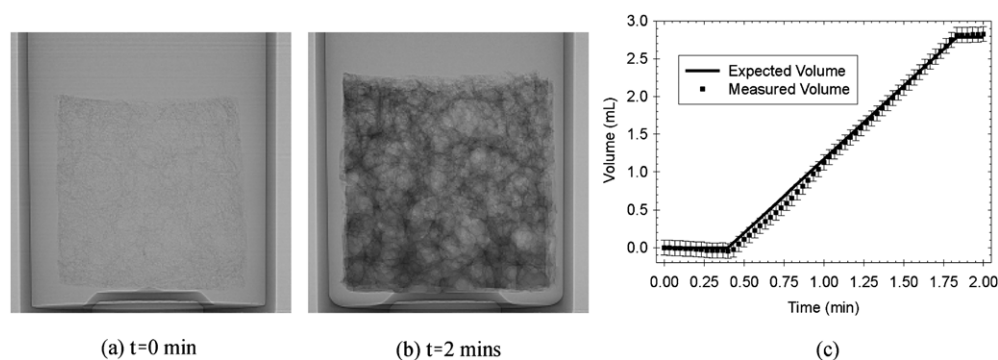


Figure 3. Phase contrast images of a (a) dry and (b) water-soaked sponge recorded using 24 keV x-rays and a 2 m object-to-detector distance. Image size: $28.6 \times 28.6 \text{ mm}^2$. Exposure time: 300 ms. Frame rate: 0.5 fps. (c) Change of water volume ($\pm 0.1 \text{ ml}$) in the sponge measured from the imaging sequence. Times given in (a) and (b) correspond to the time axis in (c).

3.2. *In situ* lung volume measurements

Figures 4(a)–(f) show a sequence of images acquired during inflations and deflations of deceased foetal rabbit pup lungs. The lungs were inflated at a fixed rate using a syringe pump and slowly deflated to atmospheric pressure. Initially, the lungs were filled with foetal lung liquid and were not visible in the images (figure 4(a)). As air entered the lungs, the airway boundaries became clearly visible due to phase contrast (figure 4(b)). At the periphery of the lung, where single small airways are in projection, the smallest air-filled sacs (alveoli, $\sim 140 \mu\text{m}$ in diameter (Hooper *et al* 2007)) became visible (figure 4(c)). Even greater visibility of the terminal airways could have been achieved using a higher resolution detector (see figure 1). However, when multiple air-filled airways overlapped in projection, a speckled intensity pattern was produced (figures 4(c)–(f)), which is caused by localized focussing effects of the air/liquid boundaries (Kitchen *et al* 2004). Continued inflation increased the visibility of the lungs due to attenuation contrast, whilst the speckled pattern continued to spread across the lungs (figures 4(d) and (e)). During deflation (figure 4(f)) the speckle pattern remained, indicating that the distal airways remained partially air filled.

The total air volume change measured using plethysmography was comparable to that measured from the images (figure 4(g)). The measurement uncertainty for the plethysmograph was determined as $\pm 0.08 \text{ ml}$ and was primarily derived from electronic noise in the amplified pressure transducer signal and the uncertainty in the system calibration. For the image analysis, the uncertainty was calculated as $\pm 0.1 \text{ ml}$ using (1) and (2), which primarily resulted from differences between the theoretical attenuation coefficient used here and the measured coefficient of water at these energies (Midgley 2005), as well as fluctuations in x-ray beam intensity. The displacement of the foetal lung liquid did not affect the airway volume calculation since this fluid remains within the imaging field of view as it is forced into the interstitial tissue spaces (Hooper *et al* 2007).

This experiment was repeated on a total of 22 pups with 17 imaged at 25 keV and the remainder imaged at 24 keV. The changes in beam energy and detector spatial resolution were accounted for in the image analysis. When data from all 22 pups were combined (>8000 measurements), the relationship between the lung air volume calculated from the images was closely related to the volumes measured using plethysmography (figure 4(h)). A least-squares linear regression analysis gave a gradient of 1.02 and an r^2 value of 0.96, demonstrating

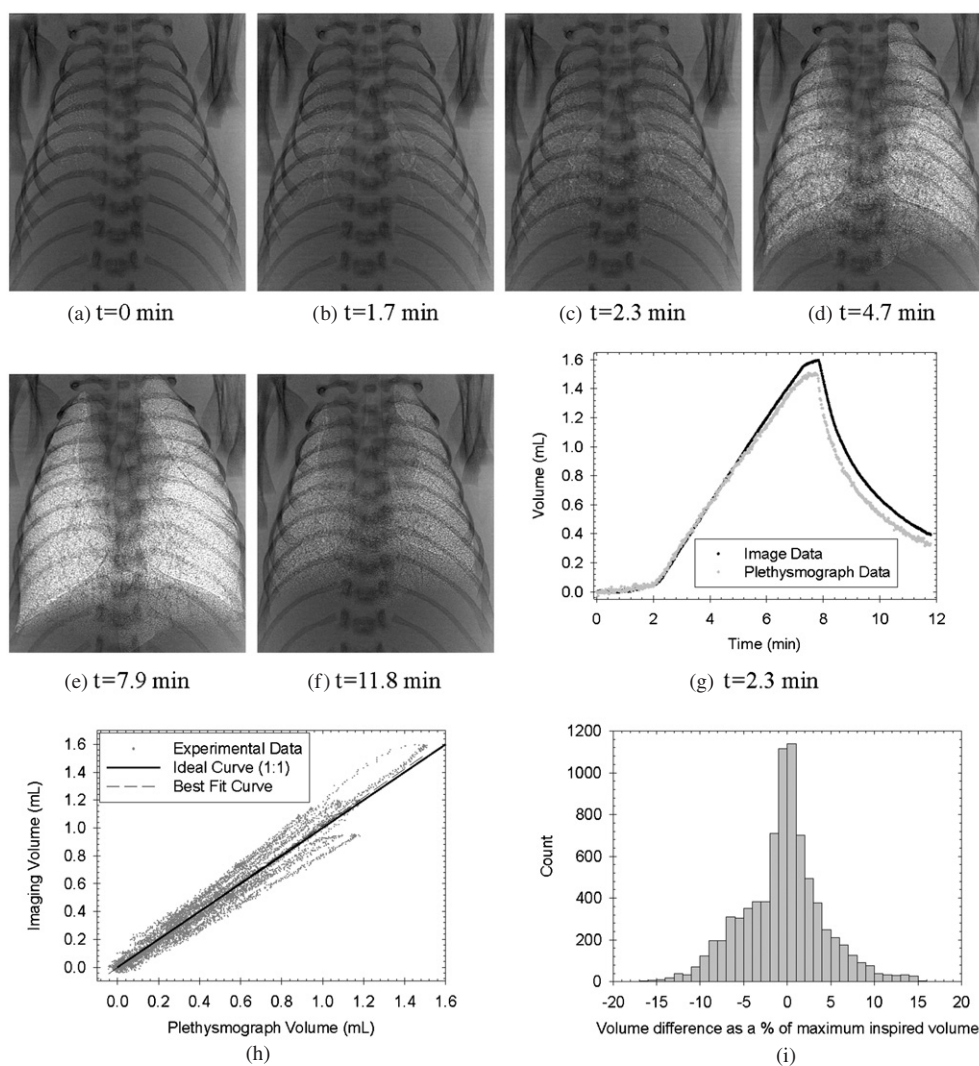


Figure 4. (a)–(f) Phase contrast imaging sequence of a deceased pup at various stages of lung inflation/deflation; peak inflation is displayed in image (e). Image size: 19.1×22.5 mm². Exposure time: 300 ms. Frame rate: 1.7 fps. Energy: 25 keV. (Movie available online at stacks.iop.org/PMB/53/6065.) (g) Change in lung air volume during inflation and deflation of the lung measured by image analysis (black) and by plethysmography (grey). Times given in (a)–(f) correspond to the time axis in (g). (h) Comparison of the lung air volume for 22 rabbit pups during inflation measured from the images and by the water plethysmograph. (i) Histogram of the differences between the image and plethysmograph volumes shown in (a) as a percentage of the maximum inspired volume.

excellent agreement between the techniques. A histogram of the differences between pairs of points (plethysmograph volume minus imaging volume) was plotted to compare the variation between techniques, as previously described (Bland and Altman 1986). This showed a mean difference of -0.007 ml with a standard deviation of 0.070 ml. Figure 4(i) shows the histogram after scaling the differences as a percentage of the maximum inspired volume of figure 4(h).

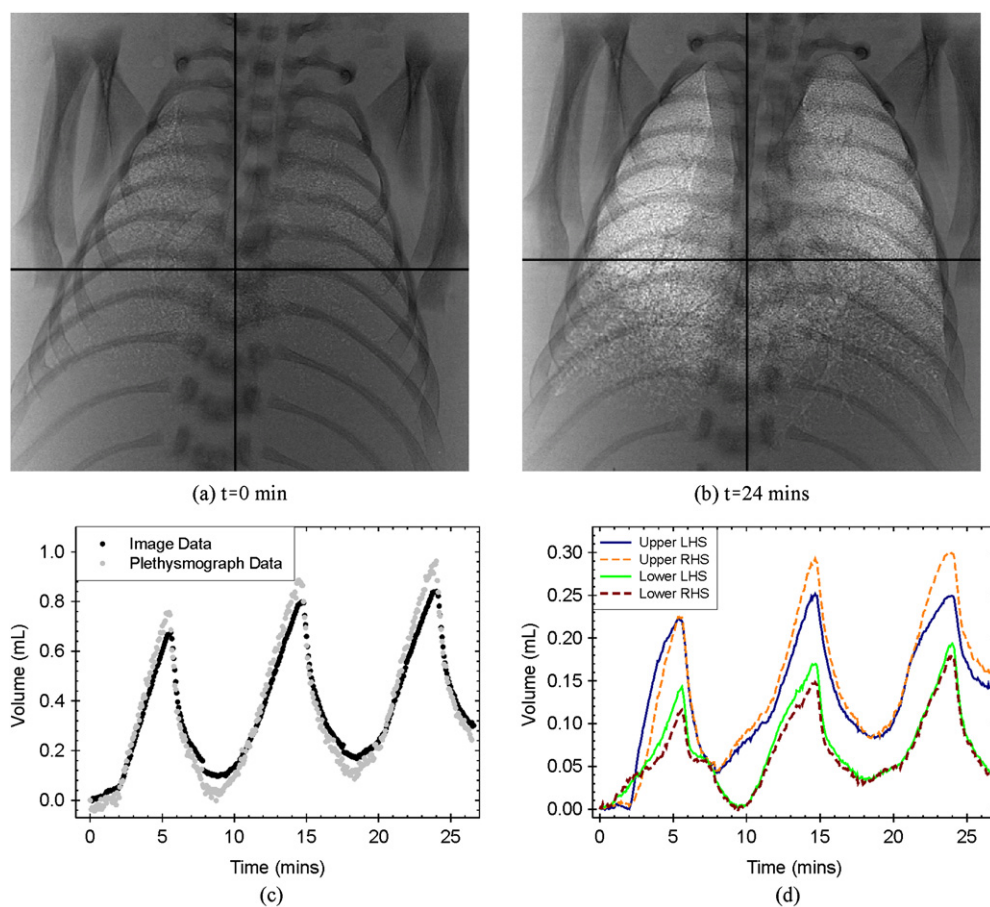


Figure 5. (a)–(b) Phase contrast images of a deceased rabbit pup at various stages of lung inflation. Image size: $22.5 \times 22.5 \text{ mm}^2$. Exposure time: 300 ms. Frame rate: 1.7 fps. Energy: 25 keV. LHS indicates the left-hand side of image and similarly for the right-hand side (RHS). (Movie available online stacks.iop.org/PMB/53/6065.) (c) Total lung air volumes measured by image analysis and plethysmography for three lung inflation/deflation cycles. (d) Regional lung air volumes measured from the lung image sequence after dividing the images into quadrants. The cross-hairs shown in (a) and (b) reveal how the quadrants move in accordance with pup motion.

This distribution has a mean of -0.45% and a standard deviation of 4.63% . The plot is slightly skewed to the left, revealing that phase contrast image analysis provided a slightly higher volume on average than plethysmography; this agrees with the gradient of figure 4(h) that is larger than unity. In addition, we estimate the lowest detectable gas volume change to be $25 \mu\text{L}$ from the images. This was calculated by taking the mean plus three standard deviations for data at zero-infused volume across all pups.

Analysis of a triple inflation/deflation loop from a deceased pup was used to illustrate how regional changes in lung gas volumes can be derived to demonstrate non-uniform rates of inflation (figure 5). Phase contrast images of the lungs at the initial time point and the maximum inflation point are shown in figures 5(a) and (b); the cross-hairs delineate the quadrants used to partition the images. Again, the total airway volumes derived by image analysis and plethysmography are in close agreement (figure 5(c)). A quadrant-based analysis (figure 5(d)) reveals that the lung segments did not aerate uniformly or at the same rate.

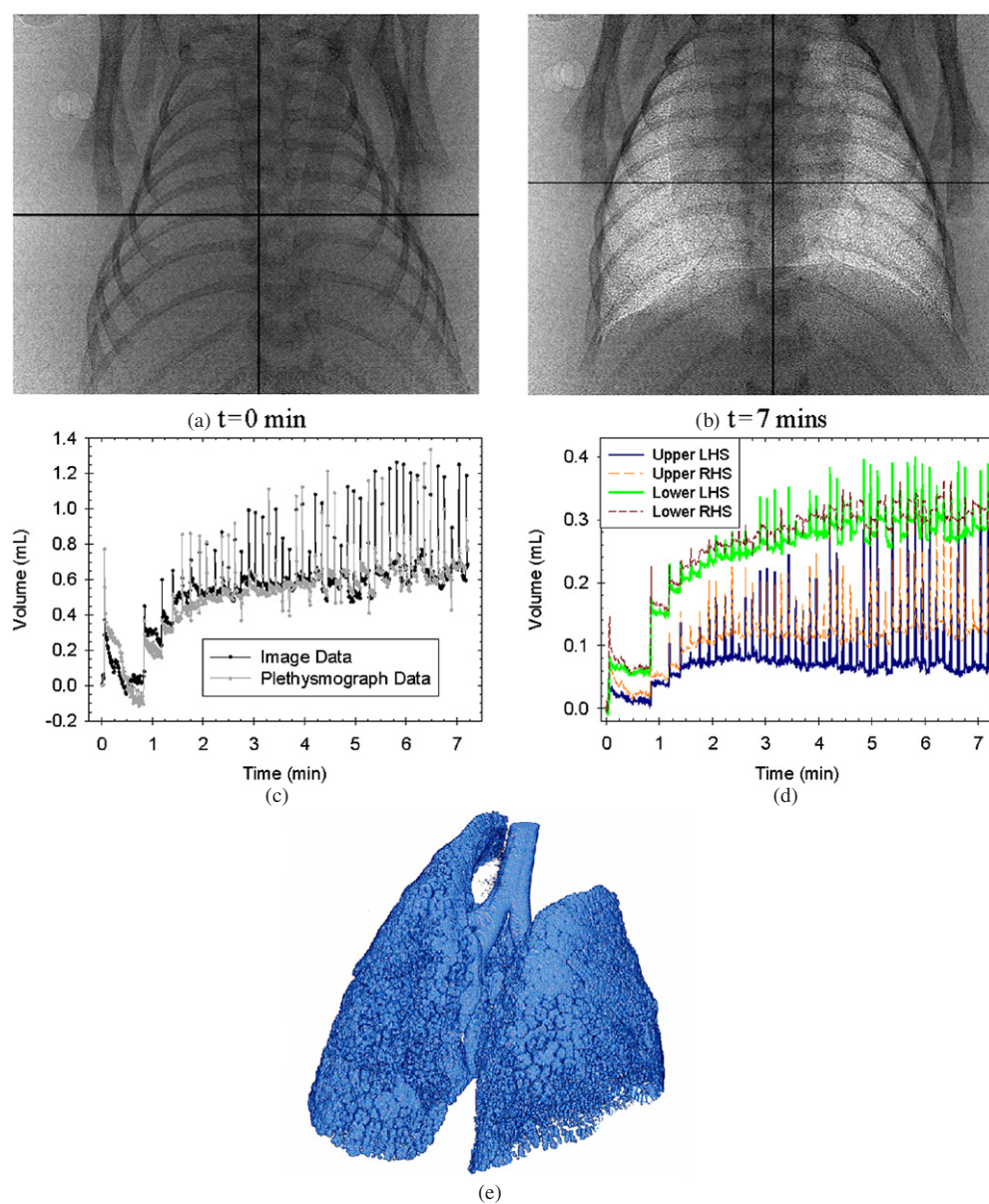


Figure 6. (a)–(b) Phase contrast x-ray image sequence of a term rabbit pup taking its first spontaneous breaths after birth. Image size: $24.7 \times 20.2 \text{ mm}^2$. Exposure time: 50 ms. Frame rate: 1.25 fps. Beam energy: 25 keV. Surface entrance dose per frame: $0.08 \pm 0.01 \text{ mGy}$. (Movie available online stacks.iop.org/PMB/53/6065.) (c) Total lung air volumes measured by image analysis and plethysmography. (d) Local volume measured from the lung imaging sequence after partitioning the images into quadrants. The cross-hairs shown in (a) and (b) reveal how the quadrants move in accordance with pup motion. (e) Rendered CT reconstruction of the airways of the pup shown in (a) and (b); images were acquired post-mortem.

Inflation began earliest in the basal (lower) lobes, but the rate and degree of inflation were greatest in the apical (upper) lobes, particularly during the first inflation. Furthermore, during

the first deflation, the basal lobes almost totally collapsed, whereas the apical lobes did not; air appeared to be displaced from the basal into the apical lobes, as indicated by an increase in apical lobe volume (between 8 and 10 min) before the second inflation began (at 9.5 min).

3.3. *In vivo* lung volume measurements

Six pups were delivered by a caesarean section, placed in the plethysmograph and imaged using 25 keV x-rays as they spontaneously aerated their lungs (figure 6). Initially, the fluid-filled lungs were not visible (figure 6(a)), but became visible as they rapidly aerated with the onset of spontaneous breathing (figure 6(b)). The rate of aeration varied markedly between pups, but was closely associated with breathing activity. Both the volume changes caused by breathing and the increase in end-expiratory gas volume (functional residual capacity (FRC)) measured using plethysmography closely matched the values measured using image analysis (figure 6(c)). A quadrant-based analysis (figure 6(d)) demonstrates that lung aeration began in the basal lobes and was more rapid there. Furthermore, the increase in FRC was much greater in the basal than in the apical lobes.

Measurements of lung air volume were also made from a high resolution CT scan (figure 6(e)) of the pup shown in figure 6, which was recorded upon killing the pup immediately after acquiring the live imaging sequence. The total airway volume was calculated to be 0.37 ± 0.02 ml. Since the live imaging recorded the pup's first breath, the lung air volume calculated from the phase contrast images and plethysmography is the absolute change in volume, which revealed an end-expiratory volume of more than 0.6 ml (figure 6(c)). Figure 6(e) reveals only partial filling of the airways, particularly in the basal lobes. This indicated that after death, lung gas volumes were reduced, possibly due to the absence of active mechanisms that neonates use, such as expiratory braking manoeuvres, to maintain lung gas volumes. This demonstrates the need to measure lung air volumes in live spontaneously breathing neonates to obtain physiologically meaningful results.

4. Discussion and conclusions

This study demonstrates that it is possible to accurately measure changes in lung air volume from a digitized sequence of high resolution x-ray images. Equations (1) and (2) reveal that this is possible with and without phase contrast; however, phase contrast can enhance the visibility of the lung by up to an order of magnitude (Kitchen *et al* 2004, 2005a, Lewis *et al* 2005), which enables airway structures and regional patterns of aeration to be directly observed. By imaging the lungs simultaneously with plethysmography, we have demonstrated that analysis of single projection phase contrast images is similar in accuracy to plethysmography for measuring total lung gas volumes. Measuring airway volume from image sequences *in vivo* also proved more accurate for determining end-expiratory lung volume than using computed tomography post-mortem.

Imaging enables the patterns of lung ventilation to be observed in near real time in spontaneously breathing animals. Unlike plethysmography, it also provides a technique for measuring regional changes in lung gas volumes. We anticipate that by tracking the displacement of specific boundaries within the lung, regional volume changes can be determined over much smaller areas of the lung. Furthermore, we currently investigate the possibilities of image segmentation to separate the bones from the soft tissues (see, e.g., Suzuki *et al* (2006), Gureyev *et al* (2002)) to provide more accurate measures of regional lung aeration.

The high volumetric resolution of the imaging technique (25 μL) suggests that it can accurately measure extremely small tidal volumes on a breath-by-breath basis. The CCD cameras and exposure times used for these experiments enable images to be captured at a rate of >5 frames per second. As spontaneous breaths lasted for 0.5–1.0 s in newborn rabbit pups (figure 6), ~5–10 images could be acquired per breath. Therefore, a detailed analysis of regional inflation could easily be obtained on a breath-by-breath basis. This would provide important biological/clinical information on the regional distribution of ventilation and compliance differences across the lung. At present, no other image-based volumetric analysis can measure lung volume changes continuously on a breath-by-breath basis and simultaneously provide a spatial resolution of less than 100 μm . Furthermore, as the surface entry dose for each image is <0.1 mGy, up to 30 breaths could be analysed in a sequence, while keeping the dose to <3 mGy. Such a low dose would make longitudinal studies feasible for examining regional changes in distal airway mechanics during the progression of lung diseases. We presently employ this technique to investigate the uniformity and distribution of ventilation in mechanically ventilated prematurely born rabbit pups from birth. Results from these animal-based experiments will provide critical information for identifying the best strategies for ventilating very preterm human infants to minimize ventilator-induced lung injury.

Acknowledgments

This work was partially funded by the Australian Research Council, the National Health and Medical Research Council of Australia, and Monash University. The authors gratefully acknowledge the SPring-8 synchrotron facility, Japan, for providing essential infrastructure. We also acknowledge the Access to Major Research Facilities Program (managed by the Australian Nuclear Science and Technology Organization) for funding the overseas visits of the Australian co-authors to Japan. M J K acknowledges insightful discussions with Dr David Paganin.

References

- Bartling S H, Stiller W, Semmler W and Kiessling F 2007 Small animal computed tomography imaging *Curr. Med. Imaging Rev.* **3** 45–59
- Bayat S *et al* 2001 Quantitative functional lung imaging with synchrotron radiation using inhaled xenon as contrast agent *Phys. Med. Biol.* **46** 3287–99
- Bland J M and Altman D G 1986 Statistical methods for assessing agreement between two methods of clinical measurement *Lancet* **1** 307–10
- Driehuys B and Hedlund L W 2007 Imaging techniques for small animal models of pulmonary disease: MR microscopy *Toxicol. Pathol.* **35** 49–58
- Ford N L, Martin E L, Lewis J F, Veldhuizen R A W, Drangova M and Holdsworth D W 2007 *In vivo* characterization of lung morphology and function in anesthetized free-breathing mice using micro-computed tomography *J. Appl. Physiol.* **102** 2046–55
- Frerichs I, Schiffmann H, Oehler R, Dudykevych T, Hahn G, Hinz J and Hellige G 2003 Distribution of lung ventilation in spontaneously breathing neonates lying in different body positions *Intensive Care Med.* **29** 787–94
- Goto S *et al* 2001 Construction and commissioning of a 215 m-long beamline at SPring-8 *Nucl. Instrum. Methods A* **467** 682–5
- Gureyev T E, Stevenson A W, Paganin D M, Weitkamp T, Snigirev A, Snigireva I and Wilkins S W 2002 Quantitative analysis of two-component samples using in-line hard X-ray images *J. Synchrotron Radiat.* **9** 148–53
- Hooper S B *et al* 2007 Imaging lung aeration and lung liquid clearance at birth *FASEB J.* **21** 3329–37
- Hu J C, Haworth S T, Molthen R C and Dawson C A 2004 Dynamic small animal lung imaging via a postacquisition respiratory gating technique using micro-cone beam computed tomography *Acad. Radiol.* **11** 961–70

- Kitchen M J *et al* 2005a Phase contrast X-ray imaging of mice and rabbit lungs: a comparative study *Br. J. Radiol.* **78** 1018–27
- Kitchen M J, Paganin D, Lewis R A, Yagi N and Uesugi K 2005b Analysis of speckle patterns in phase-contrast images of lung tissue *Nucl. Instrum. Methods A* **548** 240–6
- Kitchen M J, Paganin D, Lewis R A, Yagi N, Uesugi K and Mudie S T 2004 On the origin of speckle in x-ray phase contrast images of lung tissue *Phys. Med. Biol.* **49** 4335–48
- Lewis R A *et al* 2003 X-ray refraction effects: application to the imaging of biological tissues *Br. J. Radiol.* **76** 301–8
- Lewis R A *et al* 2005 Dynamic imaging of the lungs using X-ray phase contrast *Phys. Med. Biol.* **50** 5031–40
- Midgley S M 2005 Measurements of the X-ray linear attenuation coefficient for low atomic number materials at energies 32–66 and 140 keV *Radiat. Phys. Chem.* **72** 525–35
- Monfraix S, Bayat S, Porra L, Berruyer G, Nemoz C, Thomlinson W, Suortti P and Sovijärvi A R A 2005 Quantitative measurement of regional lung gas volume by synchrotron radiation computed tomography *Phys. Med. Biol.* **50** 1–11
- Namati E, Chon D, Thiesse J, Hoffman E A, de Ryk J, Ross A and McLennan G 2006 *In vivo* micro-CT lung imaging via a computer-controlled intermittent iso-pressure breath hold (IIBH) technique *Phys. Med. Biol.* **51** 6061–75
- NIST 2007 National Institute of Standards and Technology, Physical Reference Data, <http://physics.nist.gov/PhysRefData/XrayMassCoef/cover.html>
- Paganin D, Mayo S C, Gureyev T E, Miller P R and Wilkins S W 2002 Simultaneous phase and amplitude extraction from a single defocused image of a homogeneous object *J. Microsc.* **206** 33–40
- Schuster D P, Kovacs A, Garbow J and Piwnica-Worms D 2004 Recent advances in imaging the lungs of intact small animals *Am. J. Respir. Cell Mol. Biol.* **30** 129–38
- Suzuki K, Abe H, MacMahon H and Doi K 2006 Image-processing technique for suppressing ribs in chest radiographs by means of massive training artificial neural network (MTANN) *IEEE Trans. Med. Imaging* **25** 406–16
- Suzuki Y, Yagi N and Uesugi K 2002 X-ray refraction-enhanced imaging and a simple method for phase retrieval for a simple object *J. Synchrotron Radiat.* **9** 160–5
- Westneat M W, Betz O, Blob R W, Fezzaa K, Cooper W J and Lee W K 2003 Tracheal respiration in insects visualized with synchrotron X-ray imaging *Science* **299** 558–60
- Wilkins S W, Gureyev T E, Gao D, Pogany A and Stevenson A W 1996 Phase-contrast imaging using polychromatic hard X-rays *Nature* **384** 335–8
- Yagi N, Suzuki Y, Umetani K, Kohmura Y and Yamasaki K 1999 Refraction-enhanced x-ray imaging of mouse lung using synchrotron radiation source *Med. Phys.* **26** 2190–3